Received: 26 May 2022 | Accepted: 28 June 2022

DOI: 10.1002/mop.33405

RESEARCH ARTICLE

WILEY

Cavity length dependence on strain sensitivity for Fabry–Perot sensors

António V. Rodrigues[1,2,3] | **João Reis**[1,2] | **António José M. Martins**[4] | **Catarina S. Monteiro**[1,2,3] | **Susana O. Silva**[2] | **Cristina M. R. Caridade**[4] | **Sérgio O. Tavares**[5] | **Orlando Frazão**[1,2]

[1]Department of Physics and Astronomy, Faculty of Sciences of the University of Porto, Porto, Portugal

[2]Center of Applied Photonics INESC TEC, Porto, Portugal

[3]Engineering Physics Department, Faculty of Engineering of the University of Porto, Porto, Portugal

[4]Institute of Engineering, Polytechnic of Coimbra, Coimbra, Portugal

[5]Center for Mechanical Technology and Automation, Department of Mechanical Engineering, University of Aveiro, Aveiro, Portugal

Correspondence
António V. Rodrigues, Department of Physics and Astronomy, Faculty of Sciences of the University of Porto, Rua Campo Alegre, s/n, 4169-007 Porto, Portugal.
Email: up201008723@fc.up.pt

Funding information
Fundação para a Ciência e a Tecnologia

Abstract

This study presents the dependence of strain sensitivity on cavity length in conventional Fabry–Perot (F-P) sensors. A high number of F-P sensors were required and to ensure their reproducibility, a manufacturing process was developed to obtain similar sensors but with different types of lengths. A hollow-core silica tube was used to fabricate several F-P cavities by fusion splicing it between two sections of SMF28 fiber. The fabricated F-P has a varying length ranging from 15 to 2500 μm. The cavities were measured under a microscope and the reflected spectrum was acquired for each one. Strain measurements were performed for a maximum strain of 1000 με. The strain sensitivity showed a highly linear correlation with $\Delta\lambda_{FSR}$. Small length variations for short cavities heavily affect the FSR value. The smallest and longest cavities present sensitivities of 8.71 and 2.68 pm/με, respectively. Thermal characterization for low- and high-temperature regimes was also performed and is constant for tested sensors.

KEYWORDS

Fabry–Perot, hollow core, interferometer, optical fiber sensing, strain, temperature

1 | INTRODUCTION

Optical fiber sensing is a well-established technology, having a special interest for applications in harsh environments,[1] structural monitoring,[2,3] transportation of people and valuable goods,[4] and medicine.[5,6] Interferometric sensing is one of the more interesting technologies due to its high sensitivity. These sensors can be classified as four different designs of interferometers: Mach–Zehnder, Michelson, Sagnac, and Fabry–Perot.[7]

The main advantages of using fiber interferometers are their lightness, robustness, multi-parameter sensing capabilities, and being immune to electromagnetic interference. These characteristics confer advantages over conventional sensors.[8] Due to their multifunctionality, several fiber interferometers have been developed to assess both physical and chemical parameters of interest.[9]

Fabry–Perot (F-P) interferometers have been studied for the past decades and demonstrated, namely, in the sensing of temperature,[10] acceleration,[11,12] vibration,[13,14] pressure,[15] strain,[10,16,17] refractive index,[18] humidity,[19] magnetic fields,[20] or gas composition analysis.[21,22] The fabrication process of inline F-P interferometers using a splicing machine is a simple process that is easily repeatable. This technique can produce sensor heads for strain and temperature measurements with different characteristics depending on the cavity length.[23]

In this study, several F-P with different lengths, spanning from tenths of micrometers to a couple of millimeters, are fabricated using hollow-core silica fiber (HCF). The fabrication, control process, and study of the influence of cavity length on both cavity strain and temperature responses are presented. The characterization procedure was the same for all F-P sensors.

2 | F-P INTERFEROMETER WORKING PRINCIPLE

A F-P interferometer is formed when we observe an optical cavity with two partially reflective interfaces at both ends, as presented in Figure 1A. The light (I_i) reaches the first interface (R_1) of the cavity where a portion of the light is immediately reflected (Ir_0), and the remainder is transmitted. Inside the cavity, it propagates along its optical path length until it reaches the second interface (R_2) where the light is partially coupled out of the cavity (I_{t1}) and the remainder is reflected back. Circulating light propagates back to the first interface (R_1) where the same process happens. Interference is obtained between the first reflection (I_{r0}) and the last reflection (I_{r1}).

In the case of low reflecting interfaces, the analysis of the cavity can be reduced to a two-beam interference scenario by accounting for the first reflected beams and neglecting geometry and propagation losses. Considering an air-filled gap between silica of an optical fiber, a reflectivity of around 4% at both interfaces can be expected due to the Fresnel reflection at the index of refraction change. The first reflected beam corresponds to 4% of the initial intensity, the second beam corresponds to 3.69%, and the third beam would represent 0.006% of the total intensity. This beam has less than 600 times the intensity of both the first and second beams.[24]

In this approximation, the reflected intensity can be expressed by the following equation:

$$I_r = I_1 + I_2 - 2\sqrt{I_1 I_2}\cos\delta, \tag{1}$$

where I_1 and I_2 are the intensities of the first and second beams, and δ is the phase difference due to the longer optical path of the second beam, which performs a round-trip inside the cavity. This difference is strictly related to the cavity length and index of refraction and is described as follows:

$$\delta = \frac{4\pi n l_{\text{cav}}}{\lambda}. \tag{2}$$

This description of the cavity is characterized by a sine-modulated signal of reflected intensity. The free

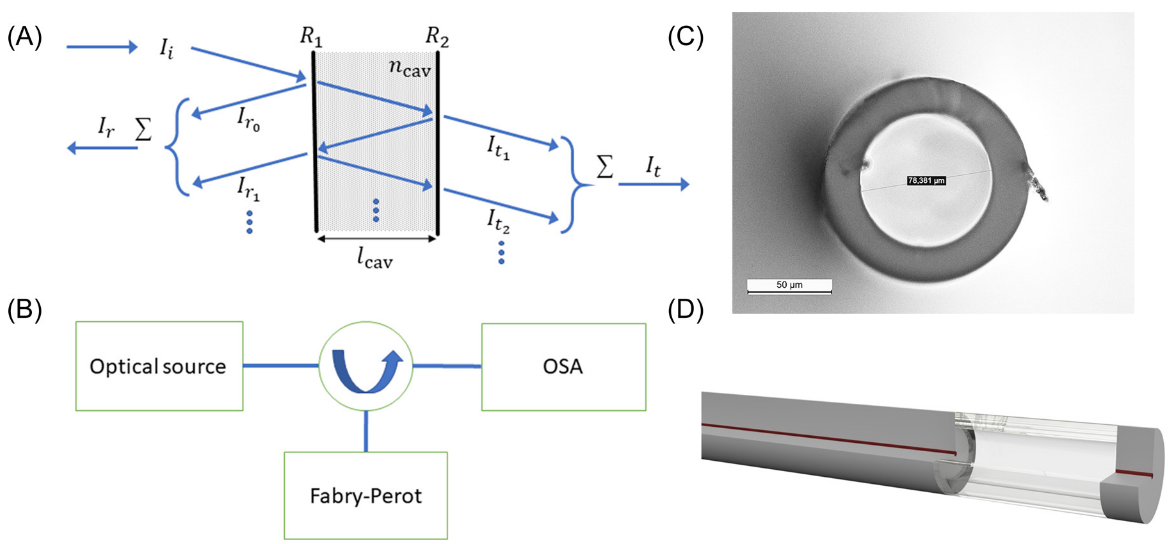

FIGURE 1 (A) Schematic of light propagation in a Fabry–Perot (F-P) optical cavity with length l_{cav} and index of refraction n_{cav}, formed between two interfaces of reflectivities R_1 and R_2. (B) Optical setup for monitoring an F-P; On the left, (C) top view of the HCF used for F-P fabrication and (D) a 3D design of single-mode fiber with an HCF F-P cavity.

spectral range (FSR) of the cavity is defined by the separation between two adjacent peaks. In this approximation, it follows from (2) and it is given as follows:

$$\Delta\lambda_{\mathrm{FSR}} = \frac{\lambda_1\lambda_2}{2nl_{\mathrm{cav}}} \approx \frac{\lambda_c^2}{2nl_{\mathrm{cav}}}. \tag{3}$$

Physical parameters, such as temperature and strain, modify the cavity parameters, changing the FSR and inducing an overall wavelength shift that can be monitored and used to assess the external parameter.

The reflection spectrum of a fiber optic F-P interferometer can be monitored using a setup as suggested in Figure 1B. In this study, a Yokogawa AQ6370C optical spectrum analyzer (OSA) with a resolution of 0.01 nm, an optical circulator, and a commercial broadband source with a spectral bandwidth of 100 nm centered at 1550 nm were used.

3 | CAVITY FABRICATION

Sensor fabrication used an HCF tube with an inner diameter of approximately 75 μm—Figure 1C,D—fusion-spliced inline with standard SMF28 fiber at both ends forming an air-filled cavity. The splices were made using a Sumitomo Type-71C in the manual splicing mode for alignment control and custom settings. Arc discharge was performed over the SMF to prevent the HCF collapse or bubble formation. Following the process depicted in Figure 2A, the first step consists of splicing one side of the HCF with the SMF, then the HCF is cleaved to the desired length for each F-P, and finally, the second face of the HCF is fusion-spliced with standard fiber as in the first step.

The second step, involving cavity length measurement, is one of the more important ones during the process if we are aiming for a given value. Usually, this stage is aided by a magnifying glass and the ruler in the cleaver, using bare hands to adjust the fiber position. To avoid trial and error, this step was adjusted. A camera was coupled with the magnifying glass, and for positioning the fiber was placed in fiber clamps and the cleaver was fitted into an XY manual translation stage. In conjunction with computer-aided measurements, this allows for a more precise cleaving process, this setup is depicted in Figure 2D.

All cavities were observed under an optical microscope for visual inspection, labeling, and cavity length measurement, examples of short and long cavities can be seen in Figure 2B. Similarly, the reflection spectrum was acquired for all F-Ps using the optical setup of Figure 1B. The FSR was measured for each cavity using multiple peaks when available. According to (3), cavity length (l_0) should present a linear behavior with the reciprocal of FSR. The relationship between measured values is presented in Figure 2B. Evaluating the change in the FSR value, the same optical path variation will cause a small change in FSR in long cavities, whereas in short cavities this change will be significantly larger. The inset of Figure 2B shows the reciprocal of cavity length and FSR, which helps verify the expected behavior, represented by the dashed curves in both plots.

4 | EXPERIMENTAL ANALYSIS

Using the optical setup of Figure 1B, each F-P interferometer was placed between two points ~0.40 m apart as depicted in Figure 3A. An acrylic adhesive was

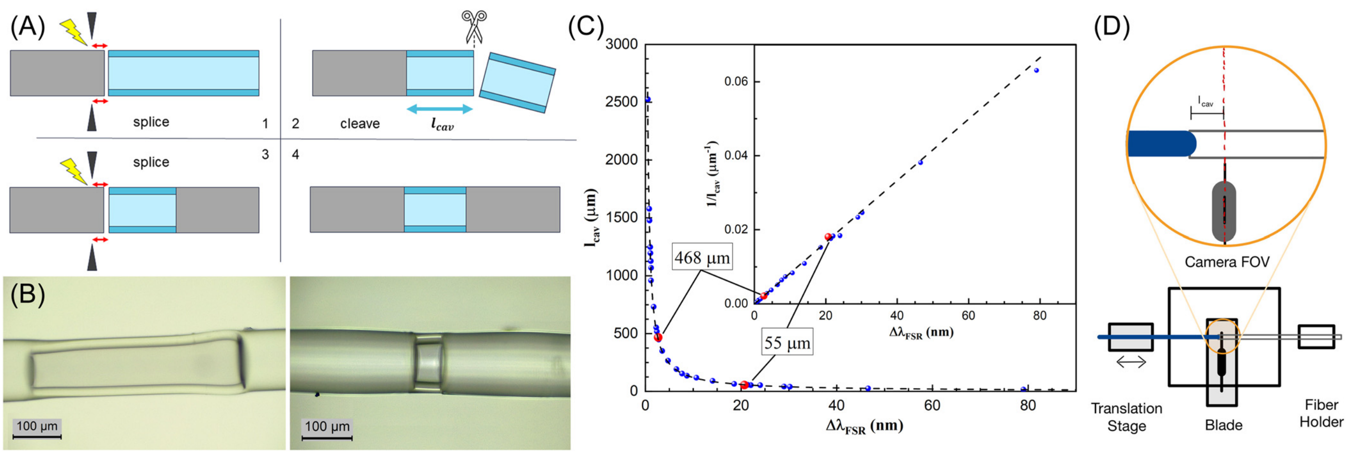

FIGURE 2 (A) Steps for fabricating a Fabry–Perot (F-P) cavity using hollow-core fiber through the fusion splicing method. (B) F-Ps under the microscope: 468-μm long (left) and 55-μm long (right). (C) Relation between measured cavity lengths and measured free spectral ranges. The theoretical dispersion for an air cavity at 1550 nm is presented in the dashed curve. (D) Schematic of the positioning setup for the precision cleaving of the cavity detailing the camera view through the magnifying glass.

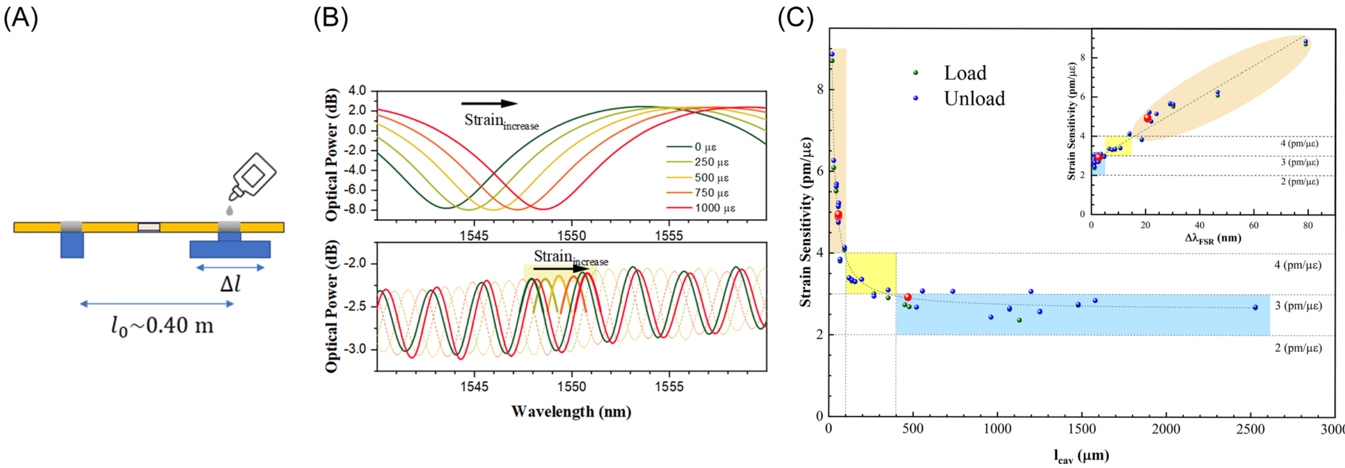

FIGURE 3 (A) Detail of the placement of the Fabry–Perot (F-P) during strain trials. (B) Spectrum evolution for applied strain variation for different F-Ps (top) 55-μm cavity; (bottom) 468-μm cavity. (C) Strain sensitivity versus cavity length and free spectral range (inset).

used to fixate the fiber on both edges. Following a similar procedure to the authors of,[23] a total inline strain was applied in the 0–1000 με range by increasing the total gauge length up to 400 μm using a linear translation stage with 1-μm resolution. Experimental data were acquired at room temperature maintaining the parameters of strain characterization for all F-Ps to ensure process uniformity.

Monitoring the wavelength shift of interference fringes on reflected spectra as strain is applied, a redshift can be observed for all characterized cavities. This behavior is presented for two cavities in Figure 3B. The maximum shift for the 55-μm cavity is greater than the maximum shift for the 468 μm one. Strain sensitivities were calculated by measuring this wavelength shift. The relationship between the calculated values with both l_{cav} and $\Delta\lambda_{FSR}$ is depicted in Figure 3C. Shorter cavities demonstrated higher sensitivities with a linear correlation with $\Delta\lambda_{FSR}$. Three zones, highlighted in the graph, can be traced out.

From larger cavities to shorter, in the light blue zone, cavities longer than 400 μm show an almost stable sensitivity averaging around 2.67 pm/με. In the light yellow zone, the sensitivity starts to escalate, and the rate of increase is greater as we go for shorter cavities. For lengths shorter than 100 μm, in the light brown zone, the sensitivity varies greatly from 4.14 to 8.71 pm/με.

After strain characterization, the cavities were subjected to thermal variation in two regimes, low- and high-temperature regimes. In the first, cavities were positioned inside an aluminum block coupled with a Peltier to control temperature. Temperature values ranged from room temperature up to ~80°C. In the second regime, a high-temperature oven was used to subject cavities to temperatures between 300°C and 500°C. Both setups are similar to the schematic presented in Figure 4A. In the low-temperature regime, not all cavities were able to be assessed because the maximum shift of the fringes was very close to the system's resolution of the measurement. Two cavities with lengths of 55 and 1070 μm were subjected to the high-temperature regime.

The temperature response of the F-Ps was kept somewhat constant for different cavity lengths, with a mean value of the temperature sensitivities, as shown in Figure 4B, as 0.84 ± 0.1 pm/°C. The cavities that were subjected to the high-temperature regime presented an average sensitivity of 0.93 ± 0.03 pm/°C (Figure 4B). The measured temperature sensitivity is in accordance with values found in the literature for the same kind of structure.[5]

The F-P stability was accessed for strain measurements at room temperature by performing a 50-min-long trial that consisted of five cycles with 5-min-long constant strain steps of 0 and 1250 με, depicted in the graph's inset of Figure 5A. The main graph shows the measurements made at 0 and 1250 με grouped by applied strain. This is the typical behavior of the produced sensors, with a stable response for constant applied strain across different load/unload cycles. In Figure 5B, the typical response of an F-P to strain variation is shown, the spectrum evolution can be seen in Figure 3B. No hysteresis could be observed during these trials.

The cross-sensitivity between strain and temperature measurements is lower for small cavities. Considering that the temperature sensitivity is constant for different cavity lengths. The cross-sensitivity is given by the ratio between the two sensitivities. The values obtained vary between 0.10 and 0.35 με/°C between small cavities to long cavities.

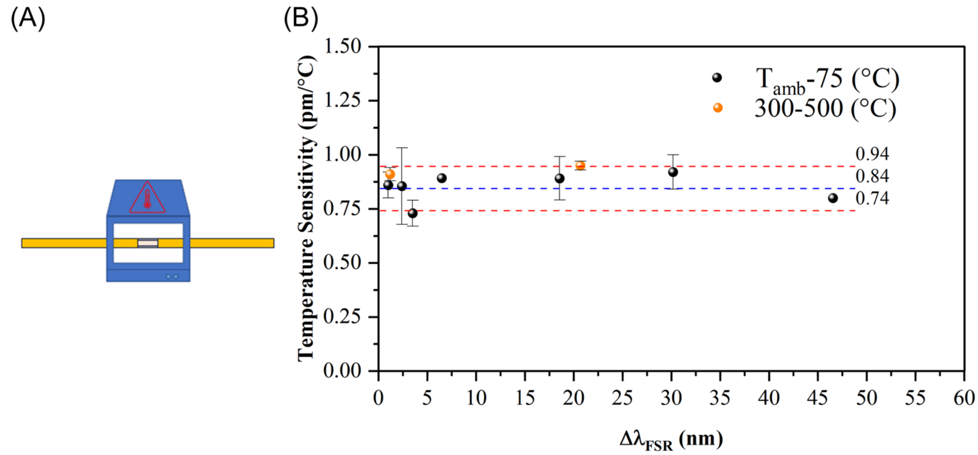

FIGURE 4 (A) Detail of the placement of the Fabry–Perot for temperature trials. (B) Temperature sensitivity versus free spectral range.

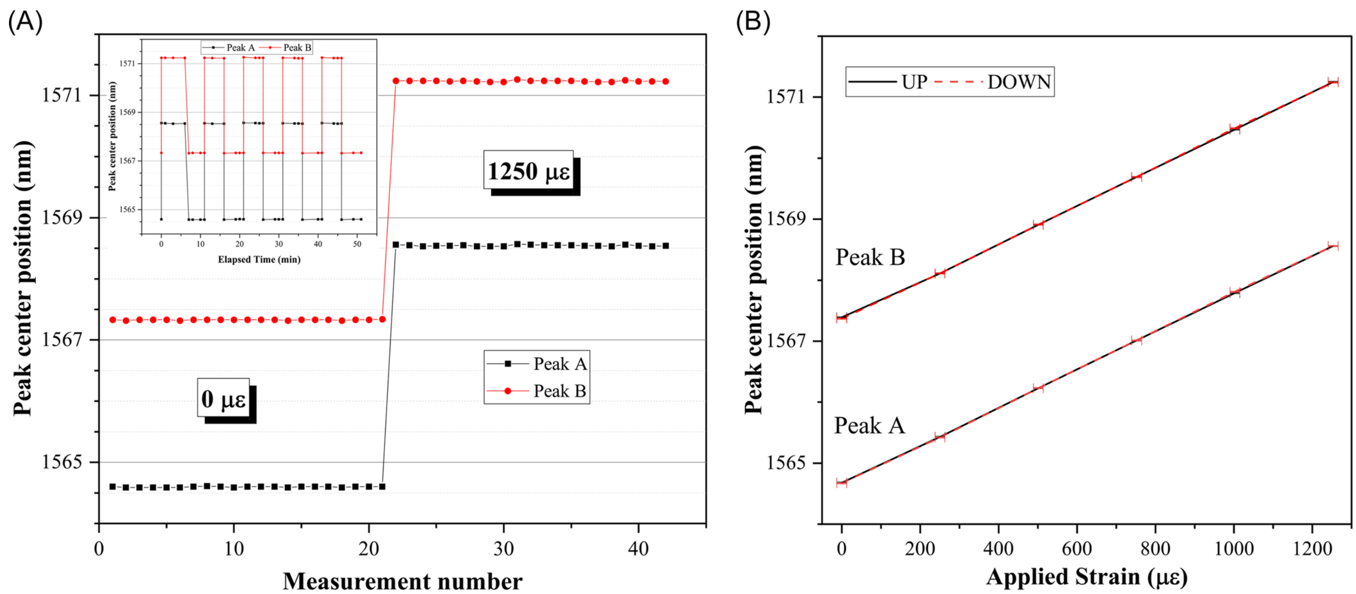

FIGURE 5 A 468-μm Fabry–Perot response for: (A) a 50-min-long stability test; (B) typical strain load/unload cycle.

5 | CONCLUSION

In this study, the different characteristics of optical fiber F-P cavities were explored. Although the fabrication process is simple, consisting of performing two splices and one cleaving step, to have good quality splices and cuts every time and to achieve the desired cavity length, some adjustments were made. Such adjustments, such as the use of fiber holders, cleaver positioning system, and video camera helped to improve the process, allowing for the fabrication of several F-P cavities with lengths in the 15–2500 μm range. The cavity length and FSR were measured under a microscope and an OSA; these values were inline with those expected for air-filled cavities. A decrease in F-P fringes visibility was verified but did not affect the behavior and analysis of the F-P mechanism. Nevertheless, the appearance of antiresonant modes suggested by Zhang et al.[25] can be an object of further studies.

A wavelength redshift was observed for interference fringes as the strain was applied. The wavelength shift itself is linear with applied strain. For the same strain, the maximum shift increased inversely to cavity length, linearly with FSR. In other words, as the F-P cavity is shortened, a greater shift magnitude is observed. The sensitivity will sharply increase for smaller cavities, which was verified for cavities shorter than 100 μm, and it will have a nearly constant value between 2 and 3 pm/με for cavities longer than 400 μm. Analysis for thermal response at high temperature has also shown a redshift, with a mean sensitivity of 0.93 ± 0.03 pm/°C. This value is also inline with the measurements of the low-temperature regime for different lengths. Thus, temperature sensitivity is shown to be independent of the cavity length.

To conclude, this study will help understand the behavior of fiber F-P interferometers to create more complex sensing structures with multiple interferometers. The developed work aims to enhance the fabrication of F-P cavities, leading to the faster fabrication of tuned sensors with better repeatability, in cases where same-length cavities are required. Considering the interests of the industry and trends of investigation, oncoming times will see a growth of smart sensing networks. Different applications may need either sensors with similar sensitivities as those for longer F-P cavities or higher sensitivities for the short ones.

ACKNOWLEDGMENTS

This study was financed by FCT — Portuguese national funding agency for science, research, and technology through António V. Rodrigues (SFRH/BD/146285/2019) and Catarina Monteiro (SFRH/BD/135820/2018).

DATA AVAILABILITY STATEMENT

The data that support the findings of this study are available on request from the corresponding author. The data are not publicly available due to privacy or ethical restrictions.

ORCID

António V. Rodrigues http://orcid.org/0000-0003-1117-5220
João Reis http://orcid.org/0000-0001-7952-9457

REFERENCES

1. Joe H-E, Yun H, Jo S-H, Jun MBG, Min B-K. A review on optical fiber sensors for environmental monitoring. *Int J Precis Eng Manuf Green Technol*. 2018;5(1):173-191. doi:10.1007/s40684-018-0017-6
2. Wang Z, Liu M, Qu Y, et al. An FBG based smart clamp fabricated by 3D printing technology and its application to incipient clamp looseness detection. Paper presented at: IEEE International Conference on Prognostics and Health Management (ICPHM). 2019:1-10, doi:10.1109/ICPHM.2019.8819399
3. Wang K, Tong X, Zhu X. Transformer partial discharge monitoring based on optical fiber sensing. *Photonic Sens*. 2014;4(2):137-141. doi:10.1007/s13320-014-0181-4
4. Wada D, Igawa H, Tamayama M, et al. Flight demonstration of aircraft fuselage and bulkhead monitoring using optical fiber distributed sensing system. *Smart Mater Struct*. 2018;2724:025014.
5. Roriz P, Silva S, Frazão O, Novais S. Optical fiber temperature sensors and their biomedical applications. *Sensors*. 2020;20(7):2113. doi:10.3390/S20072113
6. Nag P, Sadani K, Mukherji S. Optical fiber sensors for rapid screening of COVID-19. *Trans Indian Natl Acad Eng*. 2020;5(2):233-236. doi:10.1007/S41403-020-00128-4
7. Lee BH, Kim YH, Park KS, et al. Interferometric fiber optic sensors. *Sensors*. 2012;12(3):2467-2486. doi:10.3390/S120302467
8. Rajan G. *Optical Fiber Sensors: Advanced Techniques and Application*. CRC Press; 2015.
9. Islam M, Ali M, Lai M-H, Lim K-S, Ahmad H. Chronology of Fabry-Perot interferometer fiber-optic sensors and their applications: a review. *Sensors*. 2014;14(4):7451-7488. doi:10.3390/s140407451
10. Hu J, Huang H, Bai M, et al. A high sensitive fiber-optic strain sensor with tunable temperature sensitivity for temperature-compensation measurement. *Sci Rep*. 2017;7:42430. doi:10.1038/srep42430
11. Jiang J, Wang Z, Ma G, Song H, Zhang C. Direct detection of acetylene dissolved in transformer oil using spectral absorption. *Optik*. 2019;176:214-220. doi:10.1016/j.ijleo.2018.09.053
12. Zhao Z, Yu Z, Chen K, Yu Q. A fiber-optic Fabry-Perot accelerometer based on high-speed white light interferometry demodulation. *J Light Technol*. 2018;36(9):1562-1567. doi:10.1109/JLT.2017.2783882
13. Liu Z, Liu X, Zhang Z, Zhang W, Yao J. Research on optical fiber sensor localization based on the partial discharge ultrasonic characteristics in long-distance XLPE cables. *IEEE Access*. 2020;8:184744-184751. doi:10.1109/ACCESS.2020.3028765
14. Zhang G, Wu X, Li S, et al. Temperature-insensitive Fabry–Perot interferometer for microseism sensing based on hollow core photonic crystal fibres. *Opt Lasers Eng*. 2020;126:105862. doi:10.1016/j.optlaseng.2019.105862
15. Zhou X, Yu Q, Peng W. Fiber-optic Fabry-Perot pressure sensor for down-hole application. *Opt Lasers Eng*. 2019;121:289-299. doi:10.1016/j.optlaseng.2019.04.028
16. Liu S, Yang K, Wang Y, et al. High-sensitivity strain sensor based on in-fiber rectangular air bubble. *Sci Rep*. 2015;5(1):7624. doi:10.1038/srep07624
17. Novais S, Ferreira MS, Pinto JL. Fabry-Perot cavity based on air bubble for high sensitivity lateral load and strain measurements. *SPIE*. 2017;10453:204. doi:10.1117/12.2276342
18. Li X, Warren-Smith SC, Xie L, Ebendorff-Heidepriem H, Nguyen LV. Temperature-compensated refractive index measurement using a dual Fabry-Perot interferometer based on C-fiber cavity. *IEEE Sens J*. 2020;20(12):6408-6413. doi:10.1109/JSEN.2020.2976626
19. Chen M, Zhao Y, Wei H, Zhu C, Krishnaswamy S. 3D printed castle style Fabry-Perot microcavity on optical fiber tip as a highly sensitive humidity sensor. *Sens Actuators B Chem*. 2021;328:128981. doi:10.1016/J.SNB.2020.128981
20. Kendir E, Yaltkaya S. Variations of magnetic field measurement with an extrinsic Fabry-Perot interferometer by double-beam technique. *Measurement*. 2019;151:107217. doi:10.1016/j.measurement.2019.107217
21. Li Y, Zhao C, Xu B, Wang D, Yang M. Optical cascaded Fabry-Perot interferometer hydrogen sensor based on vernier effect. *Opt Commun*. 2018;414:166-171. doi:10.1016/j.optcom.2017.12.012

22. Ma J, Zhou Y, Bai X, Chen K, Guan B-O. High-sensitivity and fast-response fiber-tip Fabry–Pérot hydrogen sensor with suspended palladium-decorated graphene. *Nanoscale*. 2019;11(34):15821-15827. doi:10.1039/C9NR04274A
23. Ferreira MS, Bierlich J, Kobelke J, Schuster K, Santos JL, Frazão O. Towards the control of highly sensitive Fabry-Pérot strain sensor based on hollow-core ring photonic crystal fiber. *Opt Express*. 2012;20(20):21946. doi:10.1364/oe.20.021946
24. Rao Y-J, Ran Z-L, Gong Y. *Fiber-Optic Fabry–Perot Sensors: An Introduction*. 1st ed. CRC Press; 2017. doi:10.1201/9781315120997
25. Zhang X, Pan H, Bai H, et al. Transition of Fabry–Perot and antiresonant mechanisms via a SMF-capillary-SMF structure. *Opt Lett*. 2018;43(10):2268-2271. doi:10.1364/OL.43.002268

How to cite this article: Rodrigues AV, Reis J, Martins AJM, et al. Cavity length dependence on strain sensitivity for Fabry–Perot sensors. *Microw Opt Technol Lett*. 2022;1-7. doi:10.1002/mop.33405